Digital Discovery

Volume 1
Number 1
January 2022

rsc.li/digitaldiscovery

ISSN 2635-098X

ROYAL SOCIETY OF CHEMISTRY

ROYAL SOCIETY OF CHEMISTRY

rsc.li/digitaldiscovery

1   **Building Workflows for Interactive Human in the Loop**

2   **Automated Experiment (hAE) in STEM-EELS**

3   Utkarsh Pratiush[1], Kevin M. Roccapriore[2], Yongtao Liu[2], Gerd Duscher[1],

4   Maxim Ziatdinov[3], and Sergei V. Kalinin[1,3]

5

6   [1] Department of Materials Science and Engineering, University of Tennessee, Knoxville, TN

7   37996, USA

8   [2] Center for Nanophase Materials Sciences, Oak Ridge National Laboratory, Oak Ridge, TN

9   37831, USA

10   [3] Pacific Northwest National Laboratory, Richland, WA 99354

11

12   Exploring the structural, chemical, and physical properties of matter on the nano- and atomic scales

13   has become possible with the recent advances in aberration-corrected electron energy-loss

14   spectroscopy (EELS) in scanning transmission electron microscopy (STEM). However, the current

15   paradigm of STEM-EELS relies on the classical rectangular grid sampling, in which all surface

16   regions are assumed to be of equal *a priori* interest. However, this is typically not the case for real-

17   world scenarios, where phenomena of interest are concentrated in a small number of spatial

18   locations, such as interfaces, structural and topological defects, and multi-phase inclusions. One

19   of foundational problems is the discovery of nanometer- or atomic scale structures having specific

20   signatures in EELS spectra. Here we systematically explore the hyperparameters controlling deep

21   kernel learning (DKL) discovery workflows for STEM-EELS and identify the role of the local

22   structural descriptors and acquisition functions on the experiment progression. In agreement with

23   actual experiment, we observe that for certain parameter combinations the experiment path can be

24   trapped in the local minima. We demonstrate the approaches for monitoring automated experiment

25   in the real and feature space of the system and monitor knowledge acquisition of the DKL model.

26   Based on these, we construct intervention strategies, thus defining human-in the loop automated

27   experiment (hAE). This approach can be further extended to other techniques including 4D STEM

28   and other forms of spectroscopic imaging. The hAE library is available at (Github:

29   https://github.com/utkarshp1161/hAE/tree/main/hAE).

31 Electron energy-loss spectroscopy (EELS) in scanning transmission electron microscopy

32 (STEM)[1] has emerged as a transformative technique in modern materials science, offering an

33 unparalleled window into the structural and electronic properties[2,3] of materials at the atomic and

34 nano scales. This tool has been crucial in the development of advanced nanomaterials[4],

35 semiconductor technology, and nanoelectronics, enabling breakthroughs in these fields. It has

36 also contributed significantly to energy research, particularly in solar cells[5] and battery

37 materials[6], and in analyzing and optimizing catalysts[7] for more efficient chemical processes.

38 Furthermore, STEM-EELS has provided critical insights into plasmons in nano-optical structures

39 and the study of quasiparticles and vibrational excitations[8,9], advancing fundamental physical

40 understanding in fields like photovoltaics, sensing technologies, and solid-state physics.

41 The current paradigm of STEM-EELS is based either on single point spectroscopic

42 measurements or hyperspectral imaging on rectangular grids. For the former, human operator

43 selects the measurement locations based on the structural features observed in the structural STEM

44 image. It is also important to note that in many cases the imperfection in the scanning systems can

45 result in the misalignment between the intended and actual measurement points, leading to difficult

46 to detect errors. For the second, the region of interest is identified, and multiple EELS spectra are

47 acquired over rectangular grid of points. The resulting 3D hyperspectral data set can be analyzed

48 using physics-based methods[10] or linear[11] or non-linear dimensionality reduction methods to yield

49 2D images that are amenable to human perception and potentially interpretation. However, in this

50 approach the information is uniform over the image plane, whereas in most materials systems the

51 objects of interest are typically localized in a small number of locations. Similarly, this approach

52 is typically associated with significant beam damage and large acquisition times.

53 The limitations of the classical EELS measurements and recent emergence of the Python

54 interfaces to commercial instruments have resulted in strong interest towards automated

55 spectroscopic measurements. One such approach is based on combination of the application of

56 computer vision-based approaches to identify a priori known objects of interest and subsequent

57 spectroscopic measurements on these chosen locations.[12–15]

58 The alternative approach to automated EELS measurements is represented by the inverse

59 workflow.[14] In this, the spectral signature of interest such as specific peak positions, integrated

60 intensity, peak ratios, etc. is identified based on the prior knowledge and intended goals of the

61 experiment. This scalar measure of physical interest is referred to as the scalarizer function, and

62   the purpose of the experiment is to discover microstructural elements at which this scalarizer is

63   maximized. In this sense, DKL is targeting the exploration of physics of interest as reflected in a

64   spectrum[16]. The example of such an approach is DKL based workflows recently demonstrated by

65   Roccapriore for EELS and 4D STEM[17,18], and Liu for several SPM(Scanning probe microscopy)

66   modalities[19,20]. There is also a study which times the performance gain of the DKL in capturing

67   the spectrum-imaging which is speed's up more than $300x$[21].

68   However, until now the DKL[22] AE(Automated experiment) workflows[14,15] were realized

69   using largely ad hoc hyperparameter values chosen before the experiment. These included the

70   choice of scalarizer and acquisition functions defining exploration-exploitation balance during

71   experiment. Over the last 2 years, we have observed that the experimental path can be strongly

72   affected by these parameters, sometimes resulting in the process being stuck at selected locations

73   or exploring only one specific type of microstructural elements. This sensitivity to

74   hyperparameters and propensity to be trapped in metastable minima is well known for

75   ML(Machine learning) methods.[23,24] However, for active learning problems on the experimental

76   tools, the classical strategies for hyperparameter tuning are inapplicable. While some parameter

77   optimization can be achieved using pre-acquired ground truth data, this approach is sensitive to

78   out of distribution shift effects even for similar samples and cannot be expected to generalize for

79   different materials.

80   Correspondingly, implementation of the AE for the STEM-EELS experiments requires the

81   introduction of a different paradigm based on the interactive, or human in the loop, hAE. In this

82   hAE approach, the human operator monitors the progression of the AI-driven automated

83   experiment and introduces high-level modifications in the policies that govern the actions of the

84   machine learning agent at each step of the experiment. This integrative approach between AI and

85   human was proposed for SPM;[15] however, the nature of the possible control parameters,

86   exploration policies, and their effects on the exploration pathway has been unexplored.

87   The human-in-the-loop approach allows direct control over three critical aspects of the

88   DKL automated experiment. First, the human operator can adjust the reward function to define the

89   discovery target or specify the type of physics they are most interested in exploring. Second, the

90   human can influence the behavior of the machine learning agent, making it more or less

91   exploratory. For example, at the beginning of an experimental campaign, the operator might

92   prioritize exploratory targets, while toward the end of the session, they could narrow the focus,

93 guiding the algorithm to follow a more gradient-based approach. Finally, the human can intervene
94 to define objects or phenomena that are known a priori to be of interest. The manuscript discusses
95 how specific parameters and intervals can be adjusted to implement these steps effectively.
96 However, the overarching purpose is to present a comprehensive workflow that integrates these
97 elements. To the best of our knowledge, this represents a novel development in the community.

98 Here, we present a benchmark study across a comprehensive range of hyperparameters,
99 including local structural descriptors and various acquisition functions (AFs) tailored for both
100 exploitation and exploration phases. Additionally, we explore different AF parameters to optimize
101 our experimental setup. A pivotal aspect of our methodology involves monitoring the learning
102 progression within both the real and feature spaces of the system. The latter can in turn be defined
103 via the Variational Autoencoder (VAE[25–27]) approach. This dual monitoring provides critical
104 insights into the progression of automated experiments. Through a detailed study, we quantify
105 these observations, establishing a direct link to the pivotal role humans play in selecting the
106 appropriate parameters. This discussion further extends to potential human interventions,
107 highlighting the balance between automated processes and human expertise in optimizing
108 experimental outcomes. Our findings underscore the significance of human intuition and decision-
109 making in refining and guiding automated experimental workflows.

110
111

I.   General setting of automated experiment

113 The general setting of the STEM-EELS experiments is illustrated in **Figure 1** and can be
114 generalized for any imaging experiments based on structural and spectral images. Structural data
115 $S(x,y)$ are easy to acquire and have high density in image plane, but have relatively low information
116 density per pixel in one or few channels. In comparison, spectroscopic data $A(E)$, Figure 1b,
117 contains a wealth of information on materials properties, but acquiring spectroscopic data is time
118 consuming. Thus, by now standard approach is to acquire both the structural and the hyperspectral
119 data sets $A(x,y,E)$, Figure 1c, over rectangular grid of points. For hyperspectral data and analyze
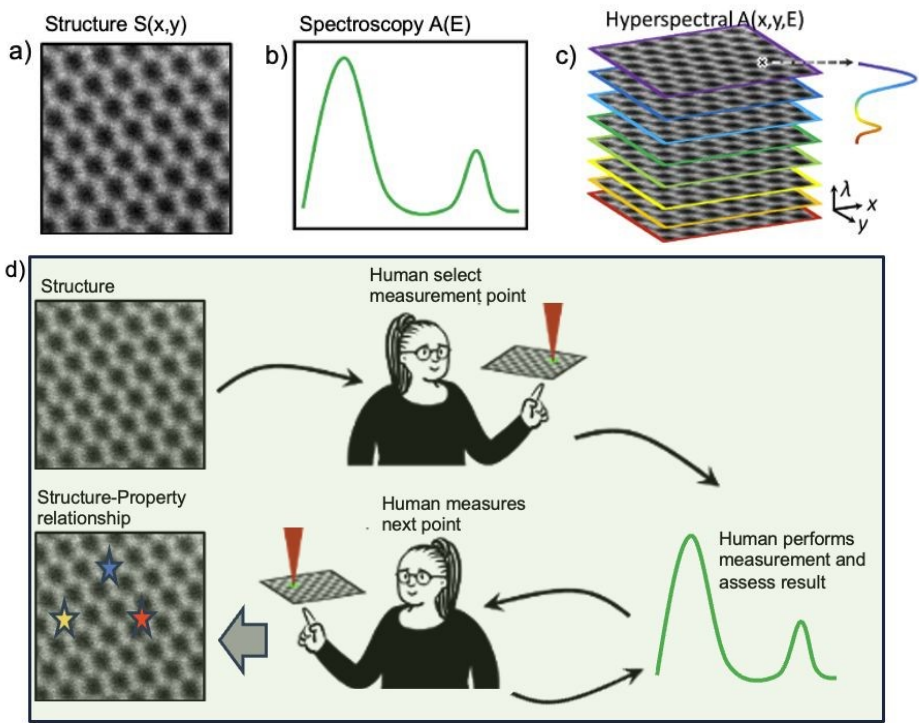120 using ML or physis based methods to get a set of 2D maps.

121

122

123

Figure 1. An example of (a) structural and (b) spectral data (coming from a single point) available in STEM. Generally, structural images are fast to acquire, whereas spectral acquisition is more time consuming. In (c) hyperspectral imaging, the spectra are acquired over dense grid, giving rise to 3D (or higher-dimensional) data set. Alternatively, (d) human selects the measurement locations based on structural elements of interest and iteratively explores image plane collecting spectral data. Overall, the goal of the experiment is to explore physical behaviors of interest visible in the spectral data using the structural images as a guide. Note that hyperspectral imaging acquires spectral data everywhere, whereas human (or ML based) feature identifications identifies location of interest based on the features visible in structural image (direct workflow). The inverse workflow as realized in DKL(**as shown in Figure 3**) solves inverse problem – discovery of structural features based on their spectral signatures of interest.

The rectangular sampling is easy to implement and, after suitable dimensionality reduction[28], is readily amenable to human perception. It is also optimal in a sense that natural way to sample unknow space if we have no prior information. However, in most cases the information of interest is concentrated in specific spatial locations. The grid-based measurements in this case

140 are sub-optimal and are associated with potential for beam damage and small explorable areas

141 because large grids result in long acquisition times longer than microscope stability allows.

142 The further development are dynamic techniques that use prior information to create

143 sampling pattern. For spectral methods, the natural approach is to use structural information to

144 identify objects of interest. One way to do it is via human selection to identify objects of interest,

145 i.e. create the locations for the spectral measurements. A similar paradigm can be implemented via

146 deep convolutional neural network (DCNN) trained on human-labeled data[13] or discovering

147 elements in the unsupervised manner[29]. Once the data is acquired, it can be analyzed to build

148 structure-property relationships, and if necessary, expanded to yield 2D images via variants of

149 inpainting, Gaussian processing[30], etc. However, this strategy relies on *a priori* knowledge of

150 which structural objects comprise the information of interest or purely on statistical properties of

151 objects in the image plane.

152 At the same time, in many scenarios it is the specific aspects of **spectral** data that we aim

153 to discover. The examples include signatures of quasiparticles, valence states, signatures of surface

154 and bulk plasmons, peaks or edge onsets corresponding to specific elements, peak ratios related to

155 the oxidation states or orbital populations, and so on.[31–33] In these cases, we can introduce the

156 measure of physical interest $A(E)$ that maps the EELS spectrum to a signature of interest. The

157 scalarizer P can be a scalar functional of spectra, or a (low dimensional) vector. Hence, a setting

158 for automated experiment is whether we aim to explore the image plane $I(x,y)$ based on the features

159 of interest in the spectra. For example, this can be learning the relationship between the structural

160 features and spectra, or discovery of structural features that give rise to certain signatures, i.e.,

161 those that maximize P. For scalar P this is optimization, for vector **P** multiobjective optimization.

162 Overall, there are three primary strategies for the spectroscopic experiments. The classical

163 approach is to acquire $\mathbf{A}(x,y,E)$ based on structural domain using a rectangular grid, shown in

164 Figure 1c. This approach is slow and associated with the beam damage to the sample. This strategy

165 is optimal when we have no other information regarding the sample (or if the structural and spectral

166 data are uncorrelated). The alternative approach is to acquire $A(E)$ manually based on structural

167 domain and supervision of human at each step, as shown in Figure 1d. This method can be

168 expensive and heavily biased by the level of expertise of the human, and strongly affected by the

169 imperfection of the positioning system. Finally, the third approach is the inverse approach. Here,

170 the goal of the experiment is to sequentially acquire EELS spectra to discover at which structural

171 elements in real space does the certain spectrum manifest. To achieve this goal, the ML algorithm

172 learns a mapping between structure domain and the spectrum domain.

173   The established approach for inverse experiment workflows is based on Deep Kernel

174 Learning[16] (DKL). To illustrate mathematical foundations of the DKL, we first consider the simple

175 Gaussian Process, defined as:

176
$$f(x) \sim \mathcal{GP}\big(m(x), k(x,x')\big) \tag{1}$$

177   In Eq.(1), $\mathcal{GP}(x)$ represents the Gaussian Process, where x is the parameter space. The $f(x)$

178 is the function we observe (e.g. image contrast). The $m(x)$ is the mean function of the GP, which

179 describes the expected value of the process at input. In typical imaging problems m is taken as

180 zero. Finally, $k(x, x')$ is the covariance (kernel) function of the GP, which models the dependencies

181 between different input points x and x'. Basically, GP represents the strategy to interpolate

182 unknown black-box function, yielding the surrogate model that predicts the function value and its

183 uncertainty over the full parameter space. These predictions and uncertainty can be further used to

184 guide the active learning over this parameter space, i.e. guide the selection of the next measurement

185 points. Bayesian Optimization is an example of such an approach, as will be discussed later.

186   Conversely, deep kernel learning learns the representation of some unknown function from

187 some high dimensional descriptor, building the correlative relationship between the two. In the

188 context of the STEM-EELS experiment, the high dimensional descriptor can be chosen to be the

189 local structure within a certain sampling window (image patch), whereas discoverable function is

190 either the full EEL spectrum or some representations of the spectrum (scalarizer).

191   A deep kernel learning[34] is defined as:

192
$$k_{DKL}\big(x_i, x_j \,\big|\, w, \theta\big) = k_{base}\big(g(x_i \,\big|\, w), g(x_j \,\big|\, w) \,\big|\, \theta\big) \tag{2}$$

193   In Eq.(2), g represents a neural network characterized by its weights w, while k_{base} denotes

194 a standard Gaussian process (GP) kernel (e.g. RBF or Matern)[35]. The neural network's parameters

195 and those of the GP base kernel are jointly learned through either Markov chain Monte Carlo

196 (MCMC) sampling methods or stochastic variational inference. Following training, the resulting

197 DKL model is employed to acquire predictive mean and uncertainty values, as well as to construct

198 the acquisition function, similar to standard GP. The difference between the two is the standard

199 GP learns to reconstruct the black-box function by iterative sampling (e.g. reconstruct the image),

200 whereas the DKL actively learns the correlative relationship between known structural and

201 dynamically explored spectral data (i.e. learn structure-property relationships).

202

II.   The DKL automated experiment

203

204   The steps of the DKL automated experiment (AE) include selection of scalarizer and

205   control of the exploration-exploitation balance via acquisition function. These elements and the

206   outputs of the AE are discussed in detail below using the pre-acquired STEM-EELS data set on

207   fluorine and tin co-doped indium oxide infrared plasmonic nanoparticles. A monochromated

208   electron beam (~50 meV full width half max) was used to access the near infrared spectral regime

209   where the plasmon resonances of these nanoparticles exist. Other relevant conditions and sample

210   preparation are reported in elsewhere;[36–38] the analysis here was performed on the data sets

211   obtained under equivalent conditions.

212

II.1. Selection of scalarizer:

213

214   By our definition, the scalarizer function defines the measure of scientist's interest to a

215   spectrum $A(E)$. In the active learning terminology, scalarizer is the myopic (i.e. available at each

216   experiment step) reward function. Scalarizer is designed with the help of the domain scientist based

217   on knowledge of the material and enabling scientists to explore the material's properties with a

218   high degree of specificity and relevance to the domain of interest. Here, we discuss the possible

219   definitions of the scalarizer function for the EELS on nanoplasmonic particles.

220   Here, the electron beam excites multiple plasmon modes within the nanoparticle cluster in

221   **Figure 2**, which exist at different locations in space and different energies. Three primary plasmon

222   modes are shown in **Figure 2**: a low energy and long-range collective mode (dipole mode - This is

223   plasmon mode of the collection of the particles), a mode confined to the particle edges (edge mode),

224   and a mode confined to nanoparticle interior (bulk mode). Since these modes occur at different

225   energies, they can be selectively imaged from a hyperspectral image by integrating the energy

226   band associated with each plasmon mode. Correspondingly, we can define a scalarizer as a spectral

227   bandpass filter: the scalarizer 1 captures dipole mode, 2 captures edge mode, 3 captures bulk

228 mode. Dependent on the experiment goals, the scalarizer function can be chosen to be more

229 complex – e.g. peak height ratio, peak width, asymmetry, and any other functional of the spectrum.
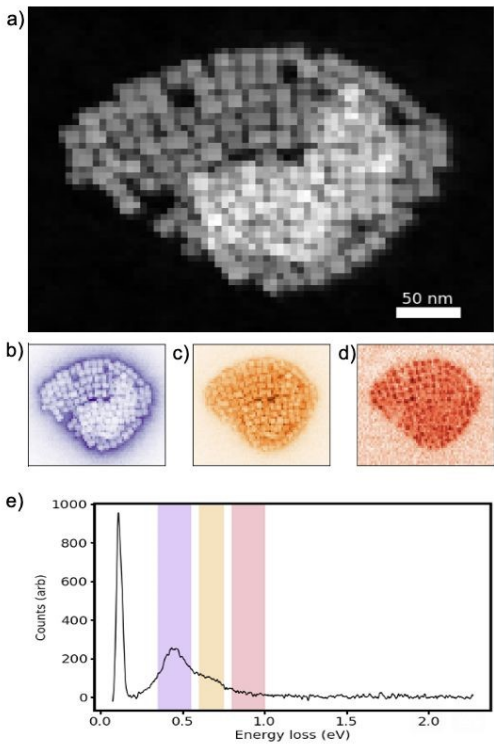
230

Figure 2. This figure represents the nanoplasmonic system: (a) is the HAADF image detailing nanoparticle structure; (b), (c), and (d) are scalarizer images representing the dipole, edge, and bulk plasmon modes, highlighting different plasmonic oscillations; and (e) is the averaged EELS spectrum, with scalarizer regions exemplified. **Note we use the terminology scalarizer 1, 2 and 3 for dipole, edge and bulk mode respectively in the paper.**

231   It is important to note that previously scalarizer was defined before the experiment.

232 However, in the interactive hAE the scalarizer can be dynamically tuned during the experiment,

233 or the type of the scalarizer can be changed. For example, the boundaries of the region of

234 integration can be dynamically adjusted, or more complex scalarizers such as peak fit parameters,

235 peak ratios, etc. can be chosen. These behaviors will be explored in the sections below.

236

237 **II.2. Policies in DKL**

238   Policy refers to a strategic approach that guides the decision process of the ML algorithm.

239   For the myopic optimization frameworks, the policy is generally built based on the estimated

240   prediction and uncertainty of prediction for unexplored parts of the parameter space, where

241   predictive model is built based on prior measurements via GP or DKL. In the context of the STEM-

242   EELS experiments, policy determines the selection of locations for new EELS measurements

243   based on structural image and results of previous EELS measurements.

244   The DKL policy is determined by the acquisition function parameters which is tuned for

245   exploration and exploitation. While the number of possible policies is large and new policies can

246   be formulated, the basic policies include expected improvement (EI), upper confidence bound

247   (UCB), and maximum uncertainty (MU). These acquisition functions[39] are explained below.

248

249   $$EI(x, \xi) = \int_{-\infty}^{\frac{(f(x_{best}) + \xi - \mu(x))}{\sigma(x)}} \left(f(x) - f(x_{best}) - \xi\right) \cdot \varphi(z)\,dz \tag{3}$$

250   Where x is the point to evaluate, $\mu(x)$ is the predictive mean, $\sigma(x)$ is the predictive standard

251   deviation, $f(x)$ the function value at (x), $f(x_{best})$ is the current best observed function value, $\phi(z)$

252   is the standard normal probability density function, and z is a standard normal random variable. ξ

253   (or xi) is the parameter that controls the trade-off between exploration and exploitation. The

254   parameter ξ in the Expected Improvement (EI) acquisition function controls the balance between

255   exploration and exploitation.

256   The expected improvement (**EI)** acquisition function (equation 3) is typically used to

257   balance exploration and exploitation. It encourages the selection of points where the predicted

258   function value is likely to improve upon the current best value. EI, measures the expected

259   improvement over the current best observation. However, in some scenarios, one might want to

260   explicitly maximize the maximum uncertainty (**MU)** to improve exploration, especially in the early

261   stages of the search or when the global structure of the function is unknown. This can help to

262   ensure a more thorough search of the parameter space and avoid premature convergence to local

263   optima.

264   Finally, the Upper Confidence Bound(**UCB)** acquisition function (equation 4) balances

265   exploration and exploitation by selecting points based on both the predictive mean and the

266   predictive standard deviation (uncertainty) of the GP model.

267

268 $$UCB(x) = \mu(x) + \delta \cdot \sigma(x) \qquad (4)$$

269 Where $\mu(x)$ is the predictive mean of the GP at point (x), $\sigma(x)$ is the predictive standard deviation

270 (uncertainty) of the GP at point (x), and δ is the UCB parameter that determines the balance

271 between **exploration and exploitation.** Note from here on we will use β(beta) instead of δ.

272   In realistic settings, the acquisition function can also include the cost of measurements.

273 This cost can be either *a priori* known, or be a discoverable function of the experiment, e.g.

274 predicted over the full image space by a separate Gaussian Process. However, in STEM EELS we

275 assume that the measurement costs are equal for all locations within the image plane.

276   Similarly to the scalarizer, the acquisition function has control parameters, e.g. exploration

277 – exploitation balance. During the automated experiment we can consider dynamically tuning the

278 acquisition function or switching between different acquisition functions. We also note that

279 spectrum acquisition can be driven by a different strategy, e.g. random selection of points or

280 sampling specific structural features. These can be switched dynamically during the experiment.

281 Like the scalarizer, this requires approaches to monitor the AE to make these decisions.

282

283 **II.3. Experiment progression and output.**

284   With the scalarizer and acquisition functions defined, we discuss the general setting of the

285 DKL experiment. The DKL based Automated experiments is summarized in a flowchart form in

286 **Figure 3** and is recommended to be referred along with the text in this section. The goal of the

287 DKL experiment is to discover which structural features in the $S(x,y)$ maximize $P = P(A(E))$. To

288 accomplish this goal, the image is represented as a collection of M patches each of size NxN,

289 where N is the patch size and M is the total number of patches. Each patch scan be indexed by

290 location (x_i,y_i), where x_i,y_i correspond to the point on the global image $S(x,y)$ from which the patch

291 has been taken. In other words, the patches are sampled over the rectangular grid. All the patches

292 are available from the beginning.

293   The microscope performs the AE on a set of seed patches (can be a single) to generate a

294 set of spectra $\mathbf{A_i}(xi,yi,E)$ and hence evaluate the scalarizer in these locations, $P(x_i,y_i)$. The seed

295 points x_i, y_i can be chosen randomly, or selected based on the analysis of the features in the global

296 image $S(x,y)$. The DKL algorithm is trained on all the patches $s(x_j,y_j)$ and the scalarizer functions

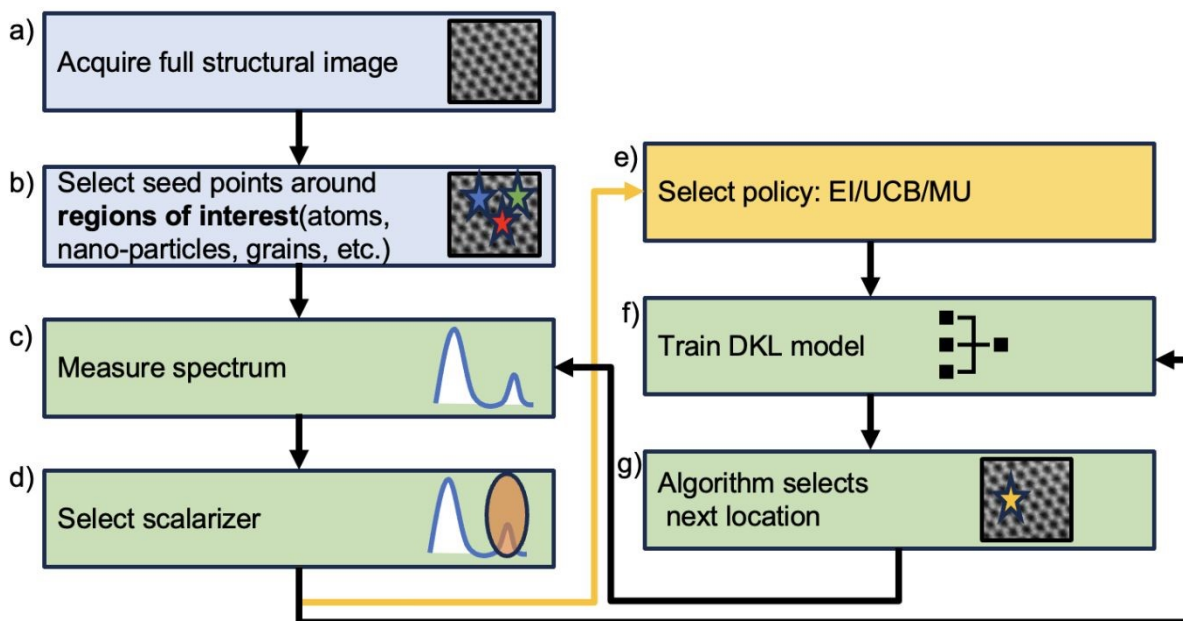297 available in the locations (x_j,y_j).

298

Figure 3. Deep kernel learning workflow: a) Acquire an image and extract patches around interesting features (atoms, nano-particles, grains, etc). b) Select seed points c) Perform spectroscopy at the seed points, generating patch-scalarizer pairs, d) Select active learning policy, f) Train deep kernel model g) Select next point based on policy. Steps c)-d)-f)-g) repeat until experimental budget. Notice e) that is policy, is set once at start of experiment.

299   After training and prediction, the DKL algorithm performs the spectral measurement in the

300   patch with coordinates:

301 $$(x_n, y_n) = \text{argmax} \, (\text{Acq}(x_i, y_i)) \tag{5}$$

302   Where i goes over all M patches (i.e. all structural descriptors). With the new measured spectrum

303    $\mathbf{A_n}(x_n, y_n, E)$, the scalarizer function, $P(A_n)$ is calculated and the DKL algorithm is retrained with

304   the additional data set. This is repeated until the expiration of experimental budget. Finally,

305   experimental trace is defined as the sequence of patches, locations, and measured spectra acquired

306   during the experiment progression.

307

308   **II.4. Additional Types of DKL experiment**

309   The output of the DKL AE is the experimental trace, or collection of the patches and

310   corresponding spectra. With the trace and after the experiment, we found it useful to define

311   several forensic tools[15] that make the understanding of the DKL easier. These include:

312 The "DKL Explore" process is designed to systematically explore a dataset using Deep

313 Kernel Learning (DKL) techniques. It begins by preparing the dataset, extracting patches and

314 associated scalarizer values, and splitting the data into training and testing sets. Over a series of

315 exploration steps, a DKL model is trained on the training data, enabling the prediction of scalarizer

316 mean and variance values for all data patches. The selection of the next data point is guided by an

317 acquisition function, which aids in identifying valuable information. The chosen data point, along

318 with its associated scalarizer value, is then added to the training data. This process is repeated for

319 each step, recording critical information such as mean, variance, selected index, acquisition

320 function value, and scalarizer value. Finally, the final training and testing datasets are saved. This

321 approach allows to simulate the DKL over pre-acquired data set, and do the initial parameter

322 tuning, reveal the relationships between the parameters, etc.

323 The "DKL Counterfactual" process conducts dataset exploration with a unique focus on

324 counterfactual scenarios within the context of Deep Kernel Learning (DKL). It initiates by

325 collecting data patches and their associated scalarizer values and establishes an initial train-test

326 split. Over each exploration step, a DKL model is trained on the existing training data to facilitate

327 the prediction of scalarizer mean and variance values for all data patches. This process employs

328 records from previous exploration steps to inform the selection of the next data point, without

329 relying on traditional acquisition function's. This counterfactual approach allows for a

330 comprehensive examination of alternative scenarios and a deeper understanding of the automated

331 experiment trajectory.

332 We have further summarized related terminology **live, final** and **complete** model required

333 to monitor knowledge acquisition in the DKL experiment in Table 1. The table also contains

334 definition to terminologies, **Latent space**, **Latent embedding** and **Latent images** which are

335 introduced later in the paper

336

337 **III. DKL on full data and the role of the window size**

338 The DKL experiment is defined in a large space of hyperparameters corresponding to the

339 selection of patch (window) sizes, scalarizer function, acquisition function, and their

340 hyperparameters. Hence, similarly to classical ML, it is advantageous to examine the effects of

341 these hyperparameters using the pre-acquired data.

342   As a first step, we have explored the effect of the varying patch sizes. We have

343   systematically explored 5,10 and 15 window sizes. Each patch is measured in terms of there area

344   whose units are pixel square. We have noted that increasing the patch size results in the change in

345   the effective resolution in the latent embedding image as shown in Figure 4[**see also**

346   **Supplementary for quantification**]. We observed a distinct scalarizer pattern emerging in the

347   DKL embedding, which indicates that DKL is effectively learning the structure-property

348   relationship inherent within the data.
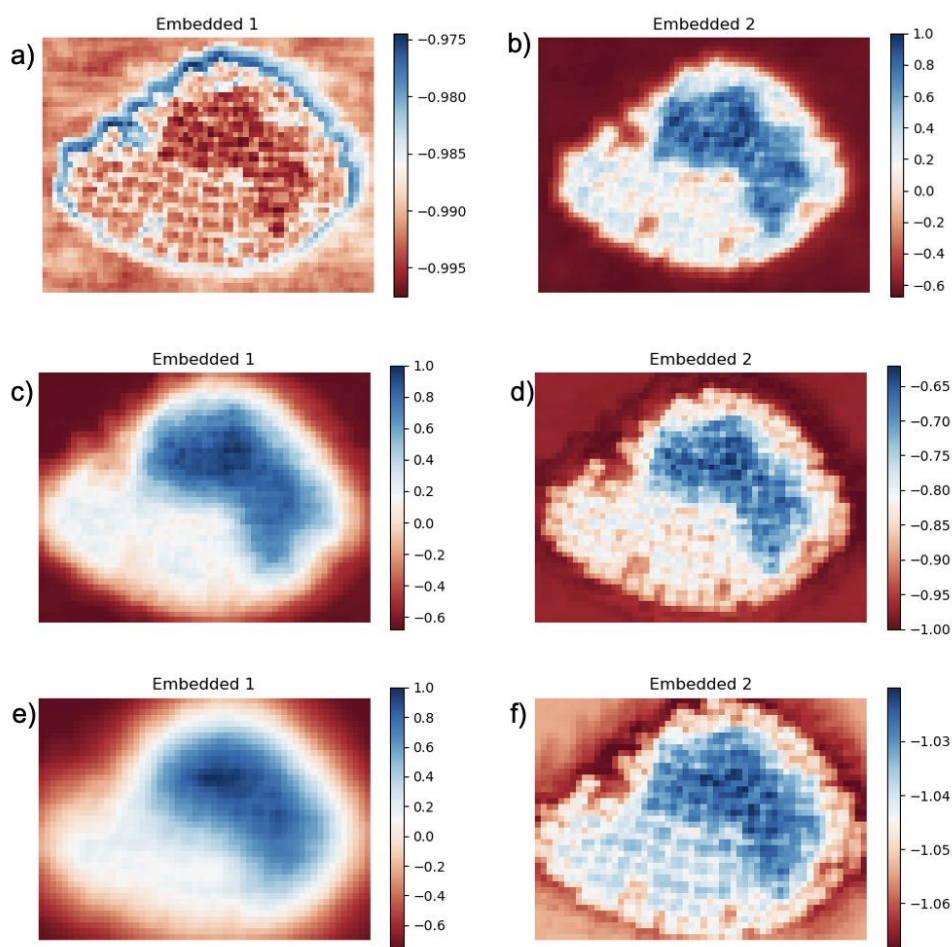
349

Figure 4 Showing DKL embedding for scalarizer "3". a) and b) correspond to patch size 5, c) and d) correspond to patch size 10, e) and f) correspond to patch size 15. See supplementary for all simulation. Here, 1 pixel corresponds to 5.10 nm.

350

351   The complementary information can be derived from the classical variational autoencoder

352   (VAE) analysis of the structural data only. Over the last several years, VAEs have emerged as a

353   powerful tool for building low-dimensional representations of data in the form of latent vectors.

354   The encoder part of the VAE compresses data to the latent vector, whereas decoder expands the

355   latent vector back to the original dimensionality, balancing the reconstruction loss and the

356   Kullback-Leibler loss between latent distribution and Gaussian. The key aspect of the VAE is their

357   capability to disentangle the factors of variability in the data, for example the width and tilt of

358   handwritten digits. These can be conveniently represented for the 2D space as latent

359   representations as shown in **Figure 5**. In this, the 2D latent space of the trained VAE is sampled

360   over 2D grid, and reconstructed objects are plotted as an image. The applications of VAEs for

361   imaging data are discussed in depth in Refs[25–27]. In particular, VAEs also allow to explicit

362   separation of invariances in data, for example rotations or translations. This comes handy in

363   microscopy images as we often visualize lattices with symmetry in both translation and rotation,

364   if the model is unaware about this inductive bias, it will have to see a lot of data to just learn

365   symmetry. Having this already encoded in model helps in better model performance in active

366   learning setup where data is already scarce. The rotationally invariant VAE (rVAE) will discover

367   the features with any rotational angle and separate it as an additional physically defined factor of

368   variation. The subfigures 5.a-c illustrate how the VAE's latent manifold changes with different

369   patch sizes 5, 10, and 15. From these visualizations, it is evident that there is less variation along

370   the y-axis (one of the latent dimensions) for a patch size of 5. This suggests that features extracted

371   from patches of size 5 contain less information compared to those from patches sized 10 and 15,

372   where both latent variables show noticeable variability. The point is that before doing the actual

373   automated experiment this analysis should be carried out to determine the ideal patch size. For

374   further details on the VAE's latent manifold definition, please refer to Table 1.

375   Here, we note that the structure of the DKL latent space is determined both by the structural

376   and spectral features. Conversely, the structure of the VAE latent space is determined only by the

377   data itself. Due its capability to disentangle the latent representations, VAE gives us access to a

378   feature space which is helpful in navigating the search space. For example, the initial selection of

379   windows size can be guided by this analysis based on structure of latent representations and

380   complexity of latent distributions. For example, we can see the scalarizer property is highlighted

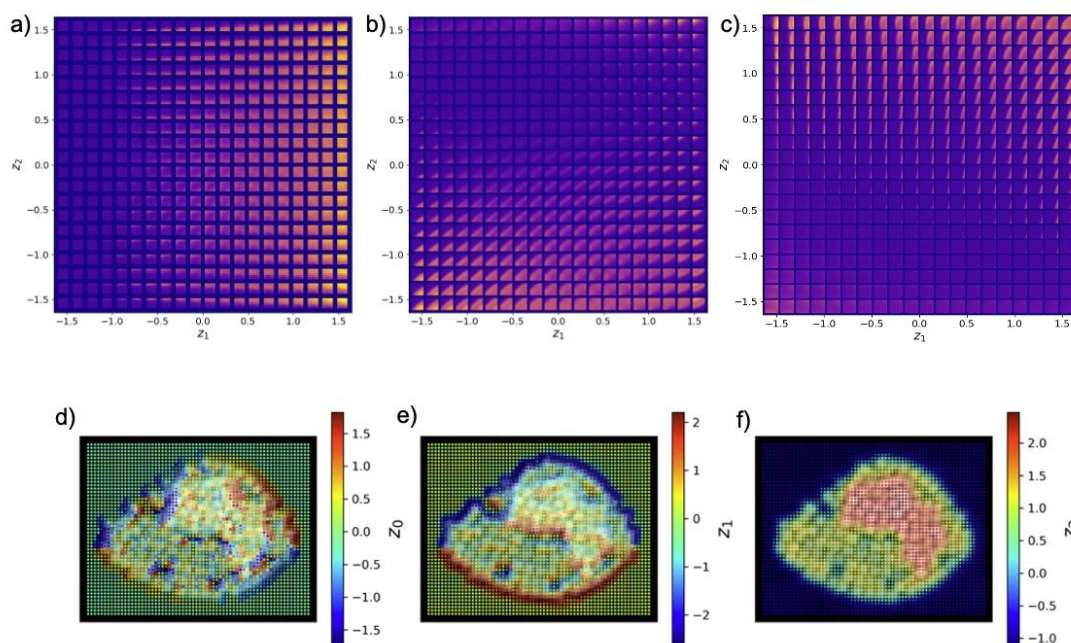381   better in embedding of DKL with patch size 5.

382

Figure 5. a), b) and c) showing latent space of rVAE for patch size 5,10 and 15 respectively. d, e and f are corresponding latent images for patch size 5. Note that the image patch can be decoded from any point in the latent space. The latent representations (top row) are generated via decoding the rectangular sampling grid in the latent space of VAE and illustrate evolution of features over the latent space. Angle latent vector is represented by z_0 in radians.

383

IV. DKL active learning

384

In DKL active learning, ML agent issues the commands to the microscope. Human operator
385 can amend the ML behavior via choice of policies and scalarizer. However, the steering of the AE
386 requires the monitoring the progression of the DKL experiments. Here we explore these
387 monitoring functions and show how hyperparameters of DKL algorithm affect the process.
388

In the actual automated experiment, we always must contend with drift, beam damage, and
389 other non-stationary effects. In order to simulate a wide range of scenarios, stress-test our system
390 under various conditions, and fine-tune the active learning algorithms to achieve optimal
391 performance here we explore the AE using the pre-acquired data.
392

393

IV.1. Monitoring learning

394

The first set of monitoring variables are directly available from the DKL itself, namely the
395 predicted scalarizer and predicted uncertainty. Note that by the nature of the DKL experiment,
396

397   these are defined for all patches within the image. Hence, for prediction and uncertainty we can

398   visualize the overall behavior, including the mean and dispersion, and explore the evolution of the

399   full distribution functions.
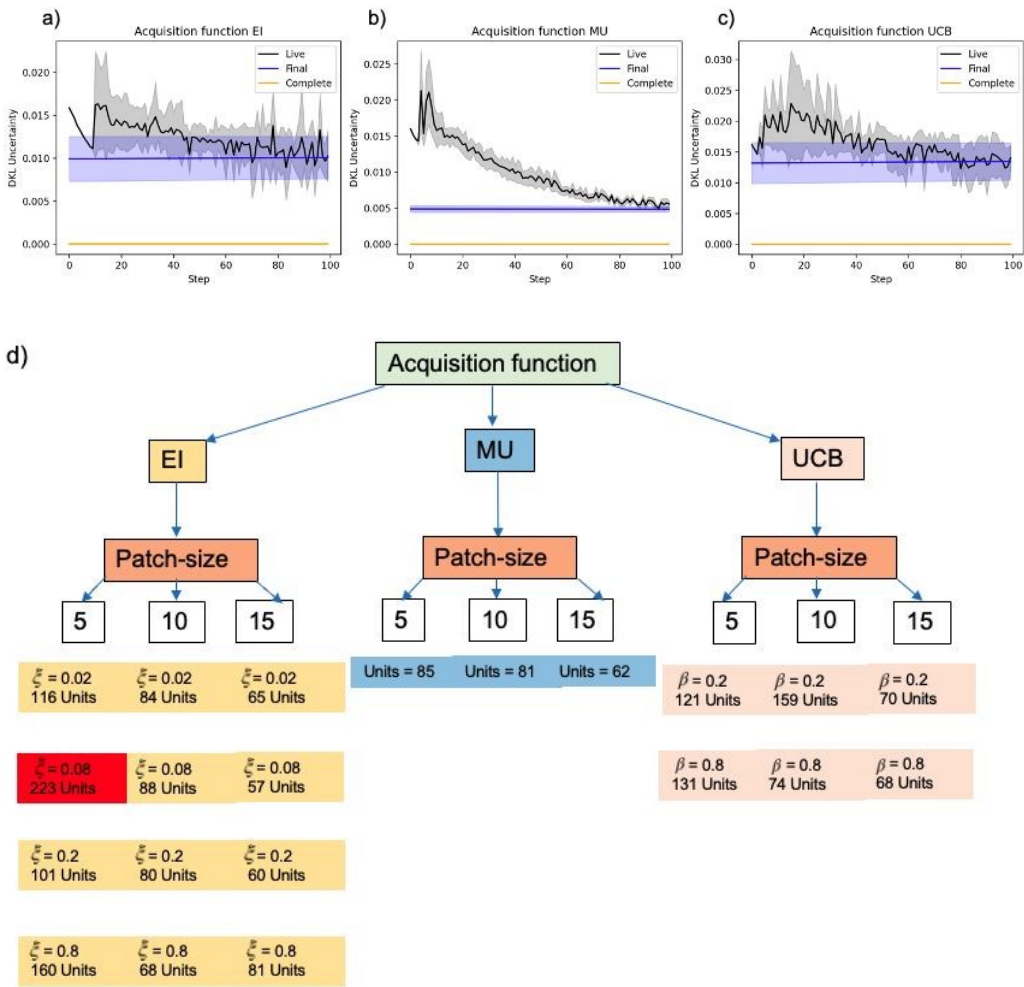
400

401

402

403

404

405

406

407

Figure 6. Monitoring learning using predictive uncertainty. a) is for acquisition function EI b) for MU and c) for UCB. Black, blue and orange curve represents live, final and complete model. The predictive uncertainty values varying "ξ" and "β" values illustrated in d). Note: The values in "d" have been scaled up by a factor of 10000. Note: The "Units" values should be seen just as a comparison based on magnitude for different "ξ" and "β values – it's not directly tied to a physical measurement but computed monitoring metric.

408

409   As an example, shown in **Figure 6** are the learning curves for the predictive uncertainty,
410   with bold black line represents mean of the prediction from the model and shaded region
411   correspond to uncertainty intervals. Here, the mean and dispersion of uncertainty are calculated
412   for all structural patches. The mean hence quantifies average uncertainty for prediction of
413   scalarized for all patches. The corresponding dispersion quantifies the distribution of uncertainties
414   over the collection of the patches. The "ξ"=0.08 is highlighted in red because it has the highest
415   predictive uncertainty among all the runs as shown in table 6d.

416   For comparison, we also show the predictions of the final and complete models. The final
417   model coincides with the live model by the end of the experiment, whereas complete model has
418   been trained on the full data (patch-spectrum pairs), and provides the comparison point for the
419   effectiveness of learning. Generally, of interest is the overall learning dynamics, namely the rate
420   of the evolution of the predictive uncertainty and its distribution, and the knowledge gain (decrease
421   of uncertainty) from the initial state and closeness to the predictions of the complete model.

422   The analysis of the learning curves for multiple scenarios as described in **Figure 8**, reveals
423   a spectrum of potential behaviors, with detailed variations outlined in the appendix. Depending on
424   the parameterization, the learning progression may exhibit a rapid decline followed by a plateau,
425   an exponential-like decrease as exemplified in **Figure 6b** or display intermittent jumps indicative
426   of sporadic learning phases. Crucially, the variance in predictive uncertainty serves as a gauge for
427   the stability of the learning process. As evidenced by the comparative analysis between **Figures**
428   **6a** and **6b,** it is apparent that the latter demonstrates a more consistent and stable learning
429   trajectory. This stability reflects the reliability of the learning algorithm in developing an accurate
430   model over the course of iterative training sessions. Such insights are invaluable for refining the
431   active learning framework, guiding the selection of parameters that foster a balance between rapid
432   convergence and consistent learning stability.

433

IV.2. Monitoring discovery

435   The second observable which aids AE is monitoring learning as described by **next step**

436 **uncertainty**, as shown in figure 7**.** Panel a), b) and c) shows how the uncertainty varies for the

437 next step over the experimental trajectory for different acquisition functions, panel d) further

438 quantifies the values, showing maximum(non-desirable) for configuration "ξ"=0.08 highlighted in

439 red. For the STEM-EELS data explored here, the evolution of the model prediction is typically

440 very noisy. We attribute this behavior to the presence of multiple geometries with almost

441 equivalent values of the scalarizer function, resulting in a very shallow landscape for the

442 acquisition function. This supposition is further confirmed in section below(**IV.3**).
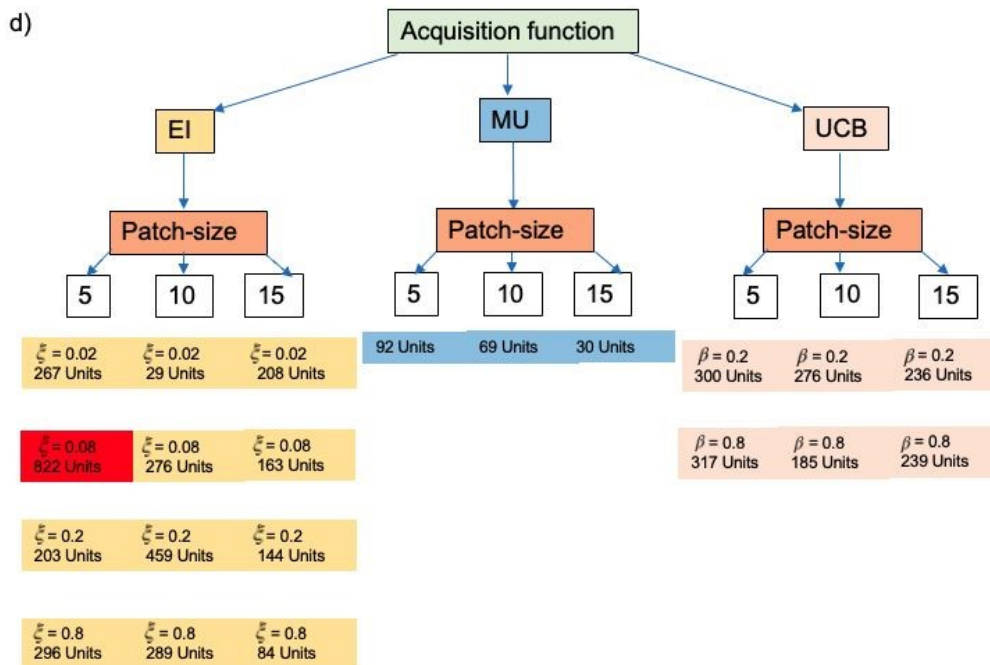
443

444

445
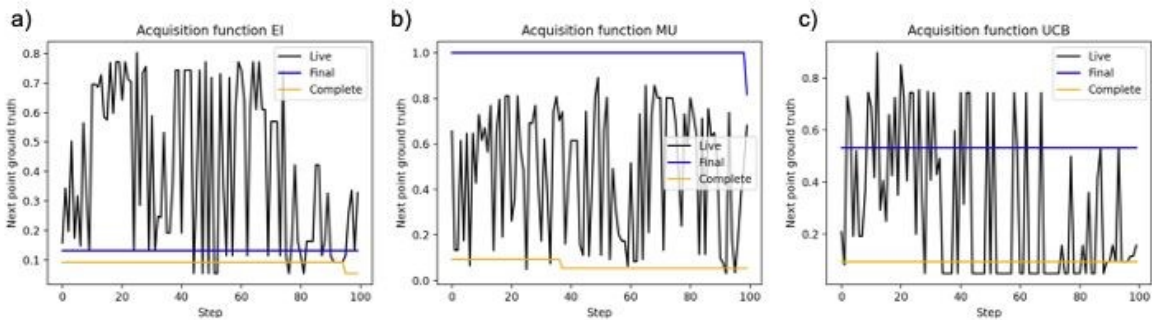
Figure 7. a), b) and c) shows next step uncertainty evolution with steps for three acquisition function. The next step uncertainty values varying "ξ" and "β" values illustrated in d). Note: The next step uncertainty values(represented as units) in "d" have been scaled up by a factor of 1000. Note: The "Units" values should be seen just as a comparison based on magnitude for different "ξ" and "β values – it's not directly tied to a physical measurement but computed monitoring metric.

446

447 **IV.3. Monitoring experimental progression in real space**

448   The third monitoring parameter that readily emerges in the context of the DKL STEM-

449 EELS experiment is the experimental trajectory in real space, i.e. the sequence of measurement

450 points selected by the algorithm. We define distance travelled in trajectory as:

451

$$\sum_i \left(\sqrt{\left(\left(x_i - x_{i+1} \right)^2 + \left(y_i - y_{i+1} \right)^2 \right)} \right) \tag{5}$$

452 where, i is trajectory point goes from 1 to 100, x_i represents movement in x direction, y_i represents
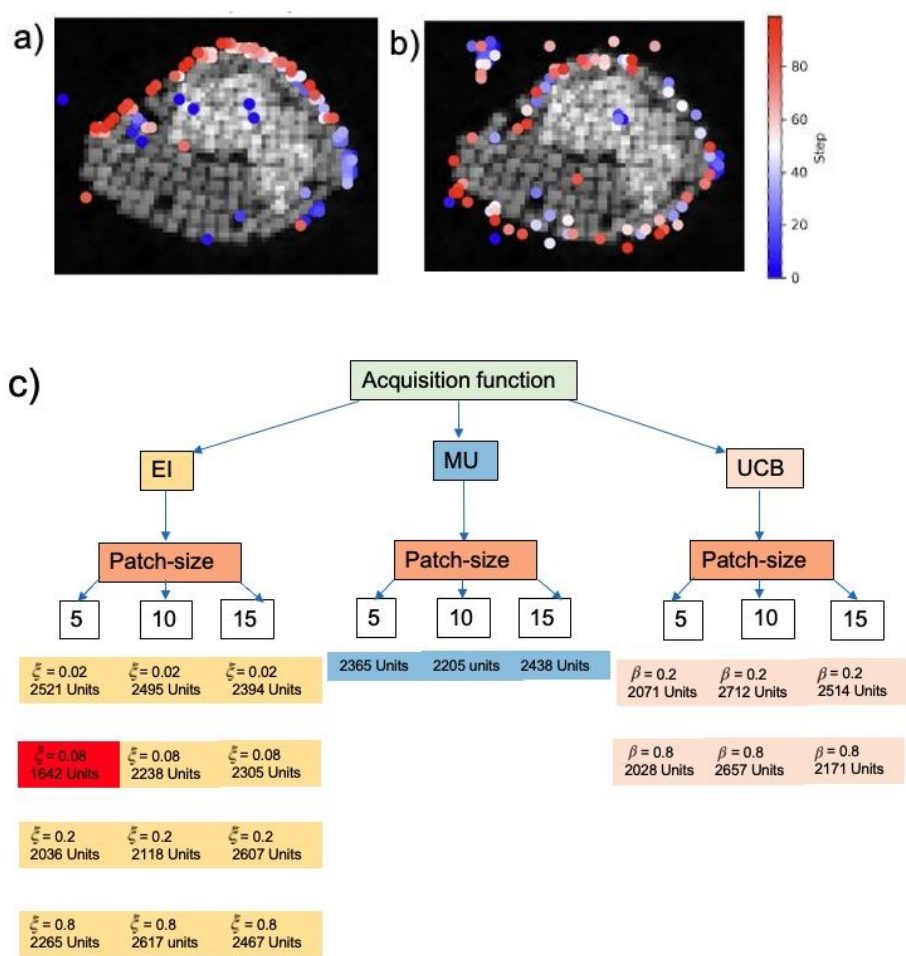
453 movement in y direction.

454

Figure 8. a) and b) showing 2 examples of AE experimental progression with acquisition function EI (ξ = 0.08, patch size =5) and EI(ξ = 0.02, patch size =10) in the simulation where trajectory exploring the edge and other getting stuck. The trajectory traversed(quantification introduced in eqn 5) values varying "ξ" and "β" values illustrated in panel d). Note: The scaling factor is applied to only the Units and is done independently for analysis presented in Figures 6,7 and 8. Also to clarify, ξ and β values are not normalized. The "Units" values should be seen just as a comparison based on magnitude for different "ξ" and "β values – it's not directly tied to a physical measurement but computed monitoring metric.

455

456   Figure 8 illustrates the monitoring of experimental progression, where: [elaborated line 455
457   onwards in the main text]

458

459   o   Subfigure (a) shows the successful navigation through regions of plasmons.

460   o   Subfigure (b) highlights the challenge of getting stuck in local minima in vacuum areas,

461   where the target property is not expected to lie. presents a process with a patch size of 10

462   and an ξ value of 0.02, resulting in a travel distance of 2495 units.

463   o   Subfigure (c) presents a metric that quantifies the travel distance, with a ξ value of 0.08

464   yielding a travel distance of 1642 units, which was the lowest and indicates that the

465   experiment did not get stuck in local minima.

466

467   These results suggest that human insight and trial can be used to carefully find ideal parameters,

468   such as the value mentioned above. The longer distance and larger patch size suggest a broader,

469   more exploratory search behavior that covers diverse regions within the parameter space,

470   potentially offering an advantage in avoiding local optima.

471

472   The examination of active learning trajectories reveals a complex relationship between the

473   learning process and the chosen hyperparameters. For most scenarios, the trajectory starts with

474   active exploration of the image space at the initial stages of the active learning. However, upon

475   exploration the trajectory can get trapped at the specific minimum. This behavior is particularly

476   often for the smaller patch sizes, as demonstrated by a patch N = 5, and Mean Uncertainty (MU)

477   policy. In contrast, larger patch sizes exhibit a lower propensity for the trajectory to become stuck

478   in the local minimum, suggesting a direct link between the patch size and the trajectory's

479   susceptibility to stagnation.

480   We note that for the explored scenarios as summarized in Figure 8 d), there is no clear

481   correlation between chosen policy, policy hyperparameters, and window sizes that can guarantee

482   the lack of local minima. In principle, one way to address this problem may be via the introduction

483   of additional components to the acquisition functions that de-prioritize the already explored areas.

484   Similarly, the acquisition function can include the cost of measurement, e.g. the time associated

485   for the traversing form one image location to the next one. We expect these additional components

486   to be highly instrument specific and to be optimized for specific instruments. However, from the

487   general perspective these additional policies will further introduce additional hyperparameters,

488   necessitating the development of both monitoring and intervention strategies, as discussed below.

489

Digital Discovery Accepted Manuscript

IV.4. Monitoring in feature space

We define the feature space of the system as the latent representation of the variational autoencoder trained on the full set of patches. This approach allows to use full power of simple, joint, semi-supervised, and conditional autoencoders to identify relevant aspects of materials structure. The detailed discussion of the VAE for materials structure exploration are discussed in multiple previous references[40,41].

We note that the capability of the VAEs to disentangle factors of variation within the data provides a very powerful tool for the exploration of the materials structure visualized via latent reorientations and latent distributions. The addition of the rotation and translation invariances naturally allows to compensate for the uncertainty in the object selection and presence of the rotational disorder in the system. Finally, semi-supervised VAE approach allows to incorporate prior knowledge on objects of interest (e.g. preferred classes), combining the classification and representation disentanglement tasks.
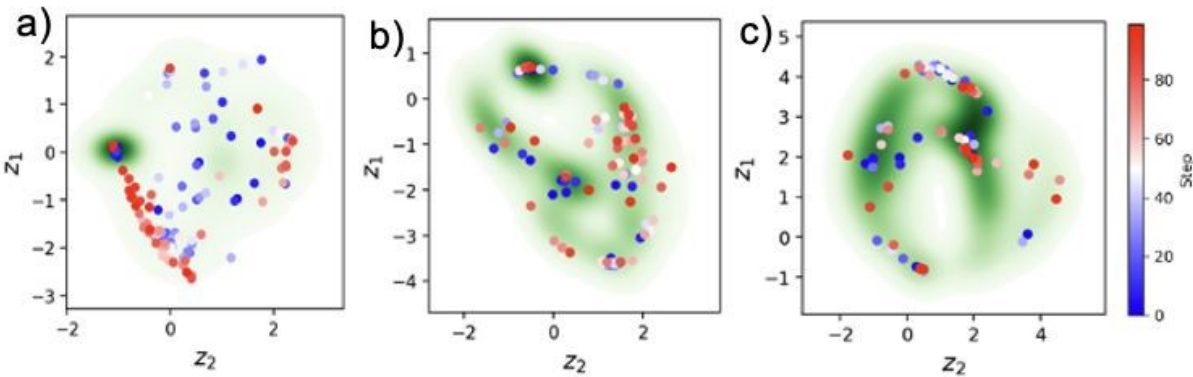

Figure 9. a), b) and c) shows example trajectory of experiment progression in rVAE latent space[see Table 1 for definition] for patch size 5, 10 and 15 respectively.

The trajectory of the automated experiment can be visualized within the Variational Autoencoder (VAE) space of the system. To analyze the distribution of points in this space, we employ kernel density estimation (KDE), which provides a smoothed representation of the underlying probability density function. The KDE allows us to identify regions with high concentrations of points, which we refer to as **"aggregation points"**. An aggregation point is defined as a location in the latent space where the kernel density estimate exhibits a local maximum, indicating a cluster or dense region of points. In the context of our experiment, we

510 observe that the latent space of the VAE exhibits distinct patterns depending on the patch size: For

511 a patch size of 5, a single aggregation point is observed, characterized by a prominent peak in the

512 kernel density estimate. For a patch size of 10, two primary aggregation points are present, with

513 kernel density estimates showing maxima at these locations, as well as several dense regions where

514 the experiment progresses. Similarly, for a patch size of 15, multiple aggregation points and dense

515 regions are evident. This behavior is intriguing, as it suggests that the latent space of the VAE

516 encodes structural information, which varies with different patch sizes. Furthermore, the

517 experiment's trajectory appears to jump between local maxima in the latent space, implying

518 transitions between distinct structural regions. This is significant, as different regions in the latent

519 space correspond to different types of structural information, providing valuable insights into the

520 system's behavior.

521

522

523 V. Interventions

524 The simulation studies above illustrate that the progression automated experiments in

525 STEM-EELS can be monitored based on the learning curves of the DKL model, real space, and

526 feature space trajectories. At the same time, for the certain parameter values the experiment can

527 be trapped in the local minima both in the real and feature spaces. The corresponding behaviors in

528 the parameter space, while demonstrating certain trends, can be highly irregular, necessitating the

529 strategies for real-time interventions during automated experiment. Note that these have to be

530 dynamic almost by definition, given the active nature of real experiment compared to the static

531 nature of the data in classical ML benchmarks (or example workflows used here).
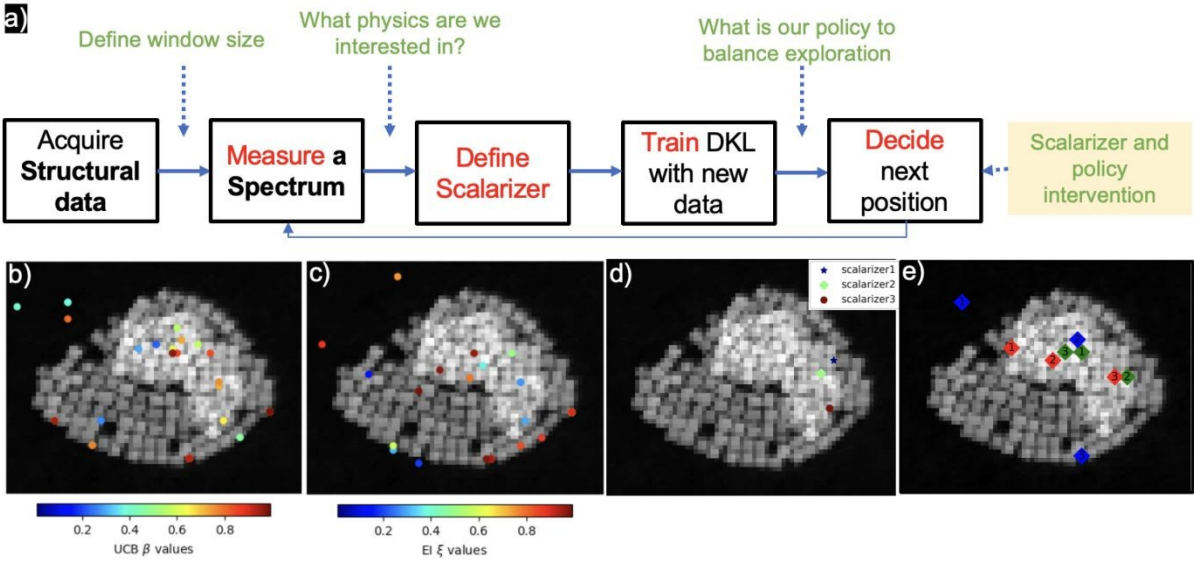
532

Figure 10.a) Shows the overall interactive experimentation flow. b) and c) shows how next point acquisition change with change in policy parameters, called **policy intervention.** Similarly, d) shows scalarization effect for next point acquisition referred to as **scalarizer intervention,** e) demonstrates scalarizer tuning effect for three tuning intervals shown for three steps.

533

534   Here, we identify the possible interventions in the DKL workflow. We note that the initial

535   step of the DKL workflow is the selection of the patch size and initial seed points. The effects of

536   the seed points have been explored by Slautin[42] .The patch size effects can be explored prior to the

537   experiment using the VAE feature space exploration, allowing the complexity of the latent

538   distribution and the nature of the disentangle factors of variations to be tuned. We further note that

539   in principle the patch size can be varied during the experiment, i.e. this is a valid intervention. This

540   is turn requires the retraining of the whole model based on the new patch size. It is important to

541   realize that in this case the full experimental trajectory prior to intervention will correspond to off-

542   policy process and can at best be considered as a new extended seed.

543   The second intervention channel is the exploration target, or scalarizer. This allows to tune

544   the relationship between the full spectrum and the myopic optimization target. The scalarizers can

545   be chosen from multiple classes (e.g. integral intensity, peak ratio, physics base reconstruction),

546   or tuned within class, e.g. change boundaries of the integrated intensity.

547   The effect of the scalarizer tuning is illustrated in figure 10 e). Here, the scalarizer is

548   integral of the EELS spectrum over an interval [a, b] where a and b can be tuned based on interested

549 physics. We note that the smooth changes in the integration boundaries result in the formation of

550 several distinct clusters of the possible future points. We attribute this behavior to relatively

551 shallow nature of the acquisition function landscape related to highly degenerate relationship

552 between the local geometries and EELS spectra. The flexibility in choice of the interval i.e. a and

553 b values lead in exploring diverse experimental trajectories converging to interesting properties.

554 Finally, the policies can be tuned on the fly via the selection and hyperparameter tuning of

555 the acquisition functions. Similarly, to scalarize, these can be visualized via the selection of the

556 Upper Confidence Bound (UCB), Expected Improvement (EI), and Maximum Uncertainty (MU),

557 or parameter tuning.

558 Shown in Figure 10 is the effect of ξ value in EI and the β value in UCB being adjusted to

559 fine-tune this balance. The scalarizer is also switched to align with the specific physics of interest,

560 such as interface, bulk, or surface plasmons, as identified by the human expert seen in d).

561

562 **VII. Summary**

563 To summarize, here we introduce the detailed framework for the human in the loop

564 automated experiment in STEM-EELS based on the myopic optimization workflows. We describe

565 the intrinsic assumptions of the myopic workflows and illustrate how it can be applied to the active

566 experiment in STEM. Based on the exploration of the broad parameter space of the system for the

567 pre-acquired data, including patch sizes, policies, and scalarizers, we demonstrate that for many

568 parameter combinations that AE can be trapped in local minima. Our comprehensive analysis, as

569 evidenced by the metrics presented in figures 6d), 7d), and 8d) (with optimal scenarios highlighted

570 in red), reveals that hyperparameter behavior can be highly localized, making it challenging to

571 identify universally effective and robust hyperparameter values. The results demonstrate that

572 hyperparameter performance can be strongly dependent on local conditions, and therefore, it is

573 difficult to determine a set of universally good and robust hyperparameter values.

574 We hence introduce the strategies of the interactive automated experiment, in which ML

575 agent issues the control signals to the microscope and the human operator monitors the progression

576 of automate experiment of the suitable time scales. To enable hAE STEM-EELS, we introduce a

577 set of monitoring functions based on the DKL model performance and real-space and feature space

578 exploration.

579   We introduce the intervention strategies for the DKL workflows based on object selection,

580   scalarizer tuning, and policy tuning. These strategies have been both operationalized and tested on

581   pre-acquired data and indicate strong degeneracies in the STEM-EELS data sets. We note that

582   while all interventions bring the experiment off policy, this allows the dynamic interaction between

583   the human operator and the microscopes.

584   Finally, we note that proposed human in the loop approach will be applicable to all other

585   myopic workflows, as long an enabling algorithm can yield predictions of function and

586   uncertainty. This includes those based on ensembled neural networks and physics-informed neural

587   networks, contextual bandits, and many other model classes. Similarly, these workflows can be

588   directly translated to other experimental tools including scanning probe microscopy, chemical

589   imaging, and combinations such as nanoindentation with optical and scanning electron

590   microscopy. As such, these developments are universal and can improve multiple areas of

591   materials science and chemical and physical imaging.

592

593   **VIII. Acknowledgements**

605

606

607 **Table 1:**

608

Term	Definition	Availability
Global structural image S(x,y)	Initial dataset of structural information was provided prior to the DKL (Deep Kernel Learning) experiment, which was utilized for generating patches to train the DKL model.	Before
Spectrum A(E)	The EELS measurement	During
Hyperspectral image A(x,y,E)	Collection of patches and spectra	During
Scalarizer function, P	Extract interested physics from spectrum	Before
Experimental trace	Spectrum and patches together	After
Acquisition function	Decides exploration or exploitation.	Before
Policy	The guiding criterion for choosing the next path in the sequence involves, at its most basic, the maximization of the acquisition function.	
Live model	The model being trained during the experiment	During
Final model	The model as soon as active learning terminates	After
Complete model	The DKL model trained from full dataset generated on grid.	NA
VAE latent	Trained on full patches	Before
Latent space	The lower-dimensional encoded space pertaining to VAE/DKL	During
Latent embeddings	The feature representation of input in the latent space	During
Latent Images	Representation of entire dataset along each of the dimensions. Number of Latent images = Number of dimensions of latent space	NA
Full DKL	Trained on complete data	NA

Learning curve	Curve showing how the DKL model behaving in active learning.	During
Monitoring curve	Curve representing next point uncertainty	During

609

610

Digital Discovery Accepted Manuscript

Digital Discovery Accepted Manuscript

References

611

612 (1) Varela, M.; Findlay, S. D.; Lupini, A. R.; Christen, H. M.; Borisevich, A. Y.; Dellby, N.; Krivanek, O. L.;
613   Nellist, P. D.; Oxley, M. P.; Allen, L. J.; Pennycook, S. J. Spectroscopic Imaging of Single Atoms
614   Within a Bulk Solid. *Phys Rev Lett* **2004**, *92* (9), 095502.
615   https://doi.org/10.1103/PhysRevLett.92.095502.

616 (2) Browning, N. D.; Wallis, D. J.; Nellist, P. D.; Pennycook, S. J. EELS in the STEM: Determination of
617   Materials Properties on the Atomic Scale. *Micron* **1997**, *28* (5), 333–348.
618   https://doi.org/10.1016/S0968-4328(97)00033-4.

619 (3) Egerton, R. F.; Malac, M. EELS in the TEM. *J Electron Spectros Relat Phenomena* **2005**, *143* (2–3),
620   43–50. https://doi.org/10.1016/j.elspec.2003.12.009.

621 (4) Nelayah, J.; Kociak, M.; Stéphan, O.; García de Abajo, F. J.; Tencé, M.; Henrard, L.; Taverna, D.;
622   Pastoriza-Santos, I.; Liz-Marzán, L. M.; Colliex, C. Mapping Surface Plasmons on a Single Metallic
623   Nanoparticle. *Nat Phys* **2007**, *3* (5), 348–353. https://doi.org/10.1038/nphys575.

624 (5) Noircler, G.; Lebreton, F.; Drahi, E.; de Coux, P.; Warot-Fonrose, B. STEM-EELS Investigation of c-
625   Si/a-AlO Interface for Solar Cell Applications. *Micron* **2021**, *145*, 103032.
626   https://doi.org/10.1016/j.micron.2021.103032.

627 (6) Yu, L.; Li, M.; Wen, J.; Amine, K.; Lu, J. (S)TEM-EELS as an Advanced Characterization Technique
628   for Lithium-Ion Batteries. *Mater Chem Front* **2021**, *5* (14), 5186–5193.
629   https://doi.org/10.1039/D1QM00275A.

630 (7) Qu, J.; Sui, M.; Li, R. Recent Advances in In-Situ Transmission Electron Microscopy Techniques for
631   Heterogeneous Catalysis. *iScience* **2023**, *26* (7), 107072.
632   https://doi.org/10.1016/j.isci.2023.107072.

633 (8) Kim, Y.-J.; Palmer, L. D.; Lee, W.; Heller, N. J.; Cushing, S. K. Using Electron Energy-Loss
634   Spectroscopy to Measure Nanoscale Electronic and Vibrational Dynamics in a TEM. *J Chem Phys*
635   **2023**, *159* (5). https://doi.org/10.1063/5.0147356.

636 (9) Zhou, W.; Lee, J.; Nanda, J.; Pantelides, S. T.; Pennycook, S. J.; Idrobo, J.-C. Atomically Localized
637   Plasmon Enhancement in Monolayer Graphene. *Nat Nanotechnol* **2012**, *7* (3), 161–165.
638   https://doi.org/10.1038/nnano.2011.252.

639 (10) Kalinin, S. V.; Lupini, A. R.; Vasudevan, R. K.; Ziatdinov, M. Gaussian Process Analysis of Electron
640   Energy Loss Spectroscopy Data: Multivariate Reconstruction and Kernel Control. *NPJ Comput*
641   *Mater* **2021**, *7* (1), 154. https://doi.org/10.1038/s41524-021-00611-8.

642 (11) Greenacre, M.; Groenen, P. J. F.; Hastie, T.; D'Enza, A. I.; Markos, A.; Tuzhilina, E. Publisher
643   Correction: Principal Component Analysis. *Nature Reviews Methods Primers* **2023**, *3* (1), 22.
644   https://doi.org/10.1038/s43586-023-00209-y.

645 (12) Roccapriore, K. M.; Ziatdinov, M.; Lupini, A. R.; Singh, A. P.; Philipose, U.; Kalinin, S. V. Discovering
646   Invariant Spatial Features in Electron Energy Loss Spectroscopy Images on the Mesoscopic and
647   Atomic Levels. *J Appl Phys* **2024**, *135* (11). https://doi.org/10.1063/5.0193607.

Digital Discovery Accepted Manuscript

648   (13)   Roccapriore, K. M.; Torsi, R.; Robinson, J.; Kalinin, S.; Ziatdinov, M. Dynamic STEM-EELS for Single-
649   Atom and Defect Measurement during Electron Beam Transformations. *Sci Adv* **2024**, *10* (29).
650   https://doi.org/10.1126/sciadv.adn5899.

651   (14)   Kalinin, S. V; Liu, Y.; Biswas, A.; Duscher, G.; Pratiush, U.; Roccapriore, K.; Ziatdinov, M.;
652   Vasudevan, R. Human-in-the-Loop: The Future of Machine Learning in Automated Electron
653   Microscopy. *Micros Today* **2024**, *32* (1), 35–41. https://doi.org/10.1093/mictod/qaad096.

654   (15)   Liu, Y.; Ziatdinov, M. A.; Vasudevan, R. K.; Kalinin, S. V. Explainability and Human Intervention in
655   Autonomous Scanning Probe Microscopy. *Patterns* **2023**, *4* (11), 100858.
656   https://doi.org/10.1016/j.patter.2023.100858.

657   (16)   Valleti, M.; Vasudevan, R. K.; Ziatdinov, M. A.; Kalinin, S. V. Deep Kernel Methods Learn Better:
658   From Cards to Process Optimization. *Mach Learn Sci Technol* **2024**, *5* (1), 015012.
659   https://doi.org/10.1088/2632-2153/ad1a4f.

660   (17)   Roccapriore, K. M.; Boebinger, M. G.; Klein, J.; Weile, M.; Ross, F.; Ziatdinov, M.; Unocic, R. R.;
661   Kalinin, S. V. AI-Enabled Automation of Atomic Manipulation and Characterization in the STEM.
662   *Microscopy and Microanalysis* **2023**, *29* (Supplement_1), 1366–1367.
663   https://doi.org/10.1093/micmic/ozad067.702.

664   (18)   Roccapriore, K. M.; Kalinin, S. V.; Ziatdinov, M. Physics Discovery in Nanoplasmonic Systems via
665   Autonomous Experiments in Scanning Transmission Electron Microscopy. *Advanced Science*
666   **2022**, *9* (36). https://doi.org/10.1002/advs.202203422.

667   (19)   Liu, Y.; Ziatdinov, M.; Kalinin, S. V. Exploring Causal Physical Mechanisms via Non-Gaussian Linear
668   Models and Deep Kernel Learning: Applications for Ferroelectric Domain Structures. *ACS Nano*
669   **2022**, *16* (1), 1250–1259. https://doi.org/10.1021/acsnano.1c09059.

670   (20)   Ziatdinov, M.; Liu, Y.; Kalinin, S. V. Active Learning in Open Experimental Environments: Selecting
671   the Right Information Channel(s) Based on Predictability in Deep Kernel Learning. 2022.
672   https://arxiv.org/abs/2203.10181.

673   (21)   Pratiush, U.; Houston, A.; Kalinin, S. V.; Duscher, G. Realizing Smart Scanning Transmission
674   Electron Microscopy Using High Performance Computing. *Review of Scientific Instruments* **2024**,
675   *95* (10). https://doi.org/10.1063/5.0225401.

676   (22)   Wilson, A. G.; Hu, Z.; Salakhutdinov, R.; Xing, E. P. Deep Kernel Learning. In *Proceedings of the
677   19th International Conference on Artificial Intelligence and Statistics*; Gretton, A., Robert, C. C.,
678   Eds.; Proceedings of Machine Learning Research; PMLR: Cadiz, Spain, 2016; Vol. 51, pp 370–378.

679   (23)   Ding, X.; Zhao, L.; Akoglu, L. Hyperparameter Sensitivity in Deep Outlier Detection: Analysis and a
680   Scalable Hyper-Ensemble Solution. In *Advances in Neural Information Processing Systems*; Oh, A.
681   H., Agarwal, A., Belgrave, D., Cho, K., Eds.; 2022.

682   (24)   Yu, T.; Zhu, H. Hyper-Parameter Optimization: A Review of Algorithms and Applications. 2020.
683   https://arxiv.org/abs/2003.05689.

684   (25)   Oxley, M. P.; Kalinin, S. V; Valleti, M.; Zhang, J.; Hermann, R. P.; Zheng, H.; Zhang, W.; Eres, G.;
685   Vasudevan, R. K.; Ziatdinov, M. Exploring Local Crystal Symmetry with Rotationally Invariant

686   Variational Autoencoders. *Microscopy and Microanalysis* **2022**, *28* (S1), 3132–3134.
687   https://doi.org/10.1017/S1431927622011655.

688   (26)   Biswas, A.; Ziatdinov, M.; Kalinin, S. V. Combining Variational Autoencoders and Physical Bias for
689   Improved Microscopy Data Analysis *. *Mach Learn Sci Technol* **2023**, *4* (4), 045004.
690   https://doi.org/10.1088/2632-2153/acf6a9.

691   (27)   Valleti, M.; Ziatdinov, M.; Liu, Y.; Kalinin, S. V. Physics and Chemistry from Parsimonious
692   Representations: Image Analysis via Invariant Variational Autoencoders. *NPJ Comput Mater* **2024**,
693   *10* (1), 183. https://doi.org/10.1038/s41524-024-01250-5.

694   (28)   Bosman, M.; Watanabe, M.; Alexander, D. T. L.; Keast, V. J. Mapping Chemical and Bonding
695   Information Using Multivariate Analysis of Electron Energy-Loss Spectrum Images.
696   *Ultramicroscopy* **2006**, *106* (11–12), 1024–1032. https://doi.org/10.1016/j.ultramic.2006.04.016.

697   (29)   Horwath, J. P.; Zakharov, D. N.; Mégret, R.; Stach, E. A. Understanding Important Features of
698   Deep Learning Models for Segmentation of High-Resolution Transmission Electron Microscopy
699   Images. *NPJ Comput Mater* **2020**, *6* (1), 108. https://doi.org/10.1038/s41524-020-00363-x.

700   (30)   Bertalmio, M.; Sapiro, G.; Caselles, V.; Ballester, C. Image Inpainting. In *Proceedings of the 27th
701   annual conference on Computer graphics and interactive techniques - SIGGRAPH '00*; ACM Press:
702   New York, New York, USA, 2000; pp 417–424. https://doi.org/10.1145/344779.344972.

703   (31)   Varela, M.; Gazquez, J.; Pennycook, S. J. STEM-EELS Imaging of Complex Oxides and Interfaces.
704   *MRS Bull* **2012**, *37* (1), 29–35. https://doi.org/10.1557/mrs.2011.330.

705   (32)   Browning, N. D.; Wallis, D. J.; Nellist, P. D.; Pennycook, S. J. EELS in the STEM: Determination of
706   Materials Properties on the Atomic Scale. *Micron* **1997**, *28* (5), 333–348.
707   https://doi.org/10.1016/S0968-4328(97)00033-4.

708   (33)   Varela, M.; Gazquez, J.; Pennycook, S. J. STEM-EELS Imaging of Complex Oxides and Interfaces.
709   *MRS Bull* **2012**, *37* (1), 29–35. https://doi.org/10.1557/mrs.2011.330.

710   (34)   Wilson, A. G.; Hu, Z.; Salakhutdinov, R.; Xing, E. P. Deep Kernel Learning. **2015**.

711   (35)   SEEGER, M. GAUSSIAN PROCESSES FOR MACHINE LEARNING. *Int J Neural Syst* **2004**, *14* (02), 69–
712   106. https://doi.org/10.1142/S0129065704001899.

713   (36)   Roccapriore, K. M.; Cho, S.; Lupini, A. R.; Milliron, D. J.; Kalinin, S. V. Sculpting the Plasmonic
714   Responses of Nanoparticles by Directed Electron Beam Irradiation. *Small* **2022**, *18* (1).
715   https://doi.org/10.1002/smll.202105099.

716   (37)   Roccapriore, K. M.; Ziatdinov, M.; Cho, S. H.; Hachtel, J. A.; Kalinin, S. V. Predictability of Localized
717   Plasmonic Responses in Nanoparticle Assemblies. *Small* **2021**, *17* (21).
718   https://doi.org/10.1002/smll.202100181.

719   (38)   Cho, S. H.; Roccapriore, K. M.; Dass, C. K.; Ghosh, S.; Choi, J.; Noh, J.; Reimnitz, L. C.; Heo, S.; Kim,
720   K.; Xie, K.; Korgel, B. A.; Li, X.; Hendrickson, J. R.; Hachtel, J. A.; Milliron, D. J. Spectrally Tunable
721   Infrared Plasmonic F,Sn:In2O3 Nanocrystal Cubes. *J Chem Phys* **2020**, *152* (1).
722   https://doi.org/10.1063/1.5139050.

723   (39)   Rasmussen, C. E. Gaussian Processes in Machine Learning; 2004; pp 63–71.
724   https://doi.org/10.1007/978-3-540-28650-9_4.

725   (40)   Oxley, M. P.; Kalinin, S. V; Valleti, M.; Zhang, J.; Hermann, R. P.; Zheng, H.; Zhang, W.; Eres, G.;
726   Vasudevan, R. K.; Ziatdinov, M. Exploring Local Crystal Symmetry with Rotationally Invariant
727   Variational Autoencoders. *Microscopy and Microanalysis* **2022**, *28* (S1), 3132–3134.
728   https://doi.org/10.1017/S1431927622011655.

729   (41)   Biswas, A.; Ziatdinov, M.; Kalinin, S. V. Combining Variational Autoencoders and Physical Bias for
730   Improved Microscopy Data Analysis *. *Mach Learn Sci Technol* **2023**, *4* (4), 045004.
731   https://doi.org/10.1088/2632-2153/acf6a9.

732   (42)   Slautin, B. N.; Liu, Y.; Funakubo, H.; Kalinin, S. V. Unraveling the Impact of Initial Choices and In-
733   Loop Interventions on Learning Dynamics in Autonomous Scanning Probe Microscopy. *J Appl
734   Phys* **2024**, *135* (15). https://doi.org/10.1063/5.0198316.

735

Data availability

The code and data for the study reported in this article can be found on zenodo repository at
https://doi.org/10.5281/zenodo.15175786

Digital Discovery Accepted Manuscript